ACS APPLIED POLYMER MATERIALS

pubs.acs.org/acsapm Article

Polyimide Aerogels with Excellent Thermal Insulation, Hydrophobicity, Machinability, and Strength Evolution at Extreme Conditions

Sizhao Zhang,* Zhao Wang, Jing Wang, Yunyun Xiao, Zhouyuan Yang, Hui Ji, Guangyu Xu, Shixian Xiong, Zhengquan Li, and Feng Ding

Cite This: *ACS Appl. Polym. Mater.* 2022, 4, 8227−8237 Read Online

ABSTRACT: High performance polyimide aerogels (PIA) are highly desirable as a part of thermal protection systems for aircraft. However, the large drying shrinkage and insufficient thermal insulation of PIA limit their practical applications in the aerospace field. Herein, the strategy of two-step prepolymerization and polycondensation route was proposed to fabricate PIA with ultralow drying shrinkage, outstanding thermal insulation, hydrophobicity, machinability, compressive strength in cryogenic/high-temperature atmospheres, flame resistance, and fantastic dimensional stability. In more detail, the drying shrinkage rate of PIA series can be lowered to 1.84%, mainly owing to the strengthened skeletons by chemical bond formation and physical entanglement of molecular chains. Excellent thermal insulation is reflected upon keeping an ink drop state as long as 265 s despite placing it on a cold surface with a temperature of −196 °C. PIA-O_2B_2 are imparted with hydrophobic properties (with water contact angle of 135°) depending on the hydrogen-bonding interaction between polyimide networking chains and 1*H*,1*H*,2*H*,2*H*-perfluorodecyltriethoxysilane that was introduced. In addition, the exceptional flame retardant is endowed completely, which is attributed to the evidence of the presence of aromatic ring structures in constructing the aerogel. The high-temperature shrinkage rate of PIA series is as low as 4.81% due to the relative small free volume of the molecular chains. Our study would provide a method for designing ultralow drying shrinkage and superb thermal insulation in cryogenic conditions for PIA in aerospace uses.

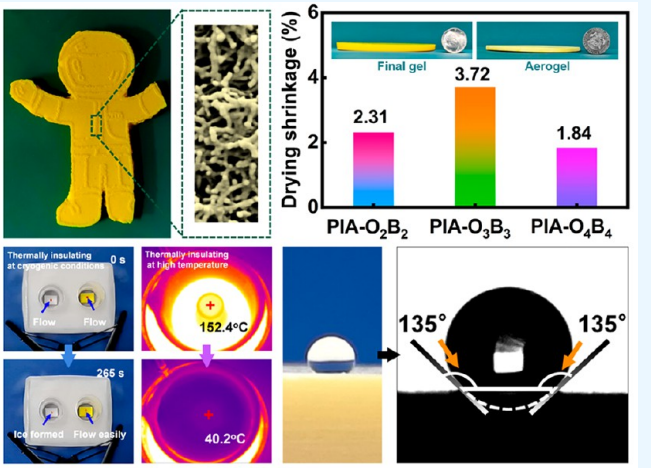

KEYWORDS: *polyimide aerogel, drying shrinkage, dimensional stability, flame retardancy, hydrophobicity*

1. INTRODUCTION

As deep exploration becomes the focus of much mainstream interests, the design and development of thermal protection systems is receiving renewed attention worldwide, which ensures the safety of human and aircraft interior facilities.[1,2] Therefore, there is an urgent need for a lightweight, low-density, high-strength, erosion-resistant, thermal protection material with excellent resistance/insulation properties. The conquest of thermal protection materials is a key core technology that cannot be avoided and must be broken through for aircraft. In recent years, more types of materials also have fabricated, such as phenolic composites,[3,4] fiber-reinforced ceramic matrix composite materials,[5−7] and aerogel composites. Phenolic composites are distinguished by their low density, low thermal conductivity, and tolerance to high temperature. However, the low elongation, brittleness, and rigidity of phenolic composites limit their potential applications. Fiber-reinforced ceramic matrix composites are known for their low thermal conductivity, low density, superior strength, and anticorrosion properties, so they are widely used in aircraft fuselage and wing lower surface thermal protection. However, the thermal stress generated within the material leads to a concentration of stresses in areas of structural incompleteness following the thermal shock, and when the thermal stress exceeds a certain value, it will lead to material failure. Aerogels are a kind of highly porous materials with lightweight and low thermal conductivity, manifesting huge

Received: July 7, 2022
Accepted: September 26, 2022
Published: October 6, 2022

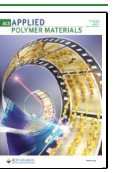

https://doi.org/10.1021/acsapm.2c01180
ACS Appl. Polym. Mater. 2022, 4, 8227−8237

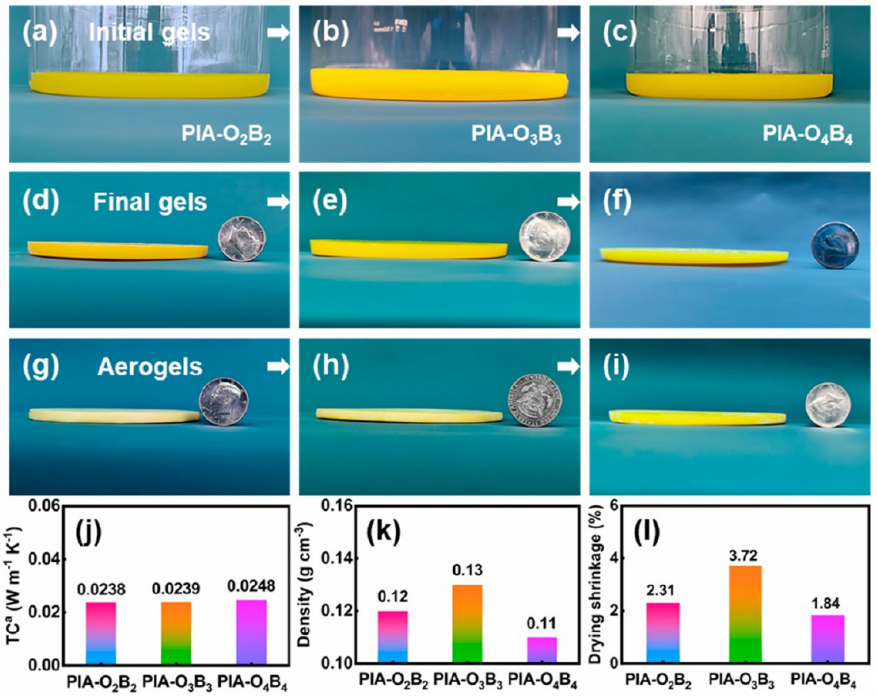

Figure 1. Samples (gels and aerogels), thermal conductivity, density, and drying shrinkage images of PIA-O_2B_2, PIA-O_3B_3, and PIA-O_4B_4. (a, d, g) PIA-O_2B_2, (b, e, h) PIA-O_3B_3, (c, f, i) PIA-O_4B_4, (j) TC^a, (k) density and (l) drying shrinkage. Notes: TC^a refers to thermal conductivity.

potentiality in various applications, particularly including thermal insulation[8] and sound insulation.[9−11]

Silica aerogels are the most welcome and the darling among these aerogels which have excellent properties such as high specific area,[12] high porosity,[13] and extremely low thermal conductivity.[14] Despite all of the advantages, their inherent fragility also affects any application.[15,16] Therefore, polyimide aerogels (PIA) are of great interest due to their ability to withstand high temperatures,[17,18] their exceptional thermal stability,[19] and their favorable mechanical properties, making PIA the material of choice in the thermal insulation field in the aerospace industry.[20,21]

At present, the matrix of PIA has the problems of large drying shrinkage and insufficient thermal insulation performance. To solve these problems, some groups have tried to introduced reinforcement and inorganic phase methods to improve drying shrinkage and thermal insulation performance. Hou et al.[22] reported that PI nanofiber cross-linked PI aerogel membranes with high flexibility, reusability, robust mechanical properties, and highly efficient thermal insulation performance had been prepared by PI nanofiber dispersion and the sol−gel method. The aerogel membranes possessed low thermal conductivity of 0.0279 W m^{-1} K^{-1} and an efficient thermal insulation property. However, the aerogel membranes had a larger shrinkage. Yu et al.[23] successfully fabricated anisotropic PI/graphene composite aerogels with a PAA ammonium salt/graphene suspension through unidirectional freezing, lyophilization, and thermal imidization. Moreover, the composite aerogel had low density (0.076 g cm^{-3}), but the thermal insulation performance was insufficient. Thus, preparing PIA that combine ultralow shrinkage with excellent thermal insulation is still a huge challenge from a practical perspective.

In this study, we launch a facile method to substantially restrain the drying shrinkage and improve thermal insulation property of PIA by introduction of prepolymers. The microstructure, thermal insulation, and mechanical properties of PIA were investigated systematically. Meanwhile, the results demonstrate that PIA endow ultralow shrinkage from final gels to aerogels, superior thermal conductivity, compressive property capable of practical applications and outstanding dimensional stability. The origin of these unique traits is also discussed from a microstructure aspect. Additionally, this study paves a way to realize the large reduction of shrinkage for PIA, conquering the challenge in the difficulty in inhibiting shrinkage. The as-prepared PIA can be a candidate for thermal protection materials in aerospace use.

2. EXPERIMENTAL SECTION

2.1. Materials. 4,4′-Oxidianiline (ODA, 98%), 3,3′,4,4′-biphenyltetracarboxylic dianhydride (BPDA, 97%), *N*-methyl pyrrolidone (NMP), oleic acid, propionic anhydride, pyridine, 1*H*,1*H*,2*H*,2*H*-perfluorodecyltriethoxysilane (PFDTES), and ethanol (AR) were sourced from Shanghai Aladdin Biochemical Technology Co, Ltd. All reagents in this work were used as received without further purification.

2.2. Fabrication of Prepolymer and Polyimide Aerogels. The prepolymer solution was synthesized by dissolving ODA, BPDA, and oleic acid in NMP. In previous literature research, N_2 is usually passed through to protect ODA from oxidation. In this work, oleic acid is used instead of N_2 to protect ODA, and the content of oleic acid is 5% of the mass of the whole solution system. The yellowish green solutions were poured into the beaker when the reaction was complete. Finally, the above solutions were placed in the water bath for programmed heating. The temperature was increased to 50 °C at the rate of 5 °C h^{-1}.

Polyimide aerogels were obtained by sol−gel method and supercritical drying method. A certain amount of ODA monomer was added into the prepolymer solution at 0 °C. After dissolution, the equimolar ratio of BPDA monomer was added to the above solution, and the polyimide acid (PAA) solution was obtained after sufficient stirring. Later, propionic anhydride and pyridine were added to the PAA solution as dehydrating agent and catalyst. The solution was transferred to the vessel after an adequate reaction time. After

https://doi.org/10.1021/acsapm.2c01180
ACS Appl. Polym. Mater. 2022, 4, 8227−8237

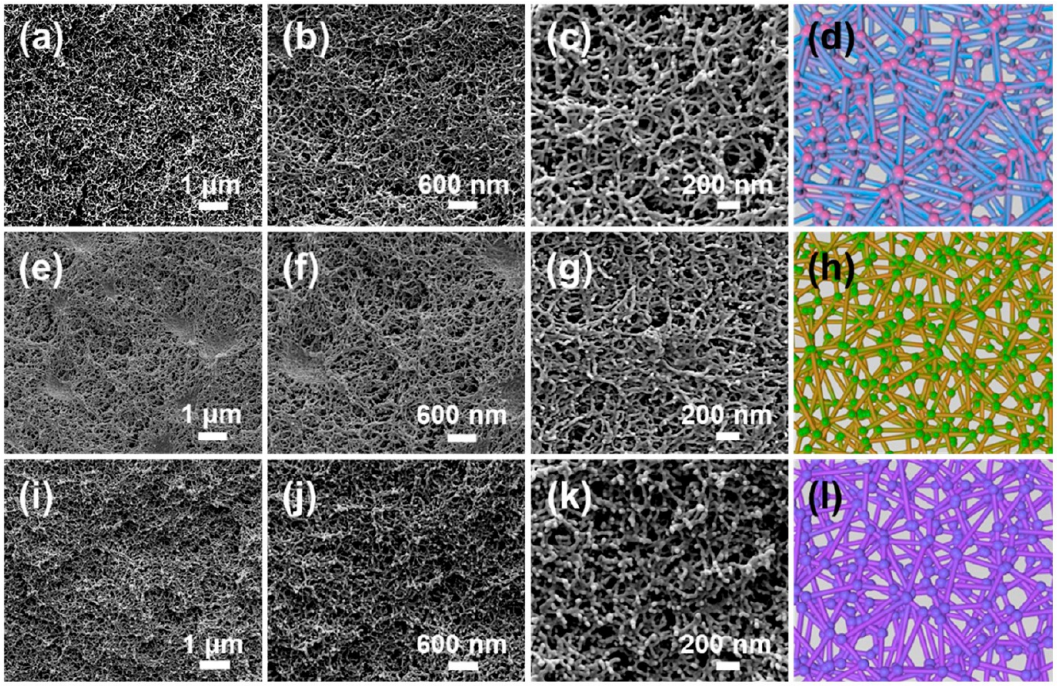

Figure 2. FESEM images and corresponding schematic diagrams of PIA series. (a–d) PIA-O_2B_2, (e–h) PIA-O_3B_3, and (i–l) PIA-O_4B_4.

gelation, polyimide gels were obtained, and the wet gels were transferred to ethanol solution for the solvent exchange process. After exchanging with ethanol for 6 times, the ethanol in wet gels were washed using supercritical CO_2 at the condition of 60 °C and 18 MPa, and then polyimide aerogels were obtained.

Eight groups of experiments were conducted according to the above methods. The sample abbreviations are follows: Because the synthetic aerogels are polyimide aerogels, the abbreviation prefix is PIA. According to the amount of ODA and BPDA prepolymerized, samples are named as PIA-O_1B_1, PIA-O_2B_2, PIA-O_3B_3, PIA-O_4B_4, PIA-O_5B_5-im sol, PIA-O_6B_6-im sol, PIA-O_7B_7-im sol, and PIA-O_8B_8. Due to the large shrinkage and poor mechanical properties of PIA-O_1B_1, the content of prepolymer was adjusted to improve it. The viscosity of the solution is naturally distributed as the content added changes. As shown in Figure S1d–f, PIA-O_5B_5-im sol, PIA-O_6B_6-im sol, and PIA-O_7B_7-im sol are unable to form gels due to excessive viscosity resulting in the failure of subsequent reagents to be added. Although a PIA-O_8B_8 sample was prepared, it was brittle. Therefore, this work chose PIA-O_2B_2, PIA-O_3B_3, and PIA-O_4B_4 to carry out the discussion and analysis.

Figure 1a–i records a complete set of images from the initial gels to the corresponding aerogels. The first row is the initial gels of PIA-O_2B_2, PIA-O_3B_3, and PIA-O_4B_4, which have smooth surfaces and the colors were yellow. The second row is the final gels, where the gel colors deepen and the hardness increases with solvent exchange. The third row is aerogels, whose color become lighter after supercritical CO_2 drying. The last row provides the corresponding thermal conductivity, the density, and the drying shrinkage, which are explained later.

2.3. Characterizations. The surface architecture and morphologies of PIA-O_2B_2, PIA-O_3B_3, and PIA-O_4B_4 were investigated using the field-emission scanning electron microscope (FESEM, FEI Inspect F50). These samples were additionally sputter coated with a gold alloy previous to being imaged. Nitrogen sorption measurements were used to measure the specific surface area of Brunauer–Emmett–Teller (BET) in N_2 environment, and the pore size distribution (in desorption branches) of Barrett–Joyner–Halenda (BJH) was obtained with Quadra Sorb SI analyzer. The degassing temperature was 90 °C, and the degassing time was 12 h. Fourier-transform infrared spectra (FTIR, Thermo Scientific Nicolet iS5) of all dried PIA-O_2B_2, PIA-O_3B_3, and PIA-O_4B_4 were calculated on a spectrophotometer with KBr pressure spheres in the range of 400–4000 cm^{-1}. The composition of PIA-O_2B_2, PIA-O_3B_3, and PIA-O_4B_4 was measured by an X-ray photoelectron spectrometer (XPS, Thermo Scientific K-Alpha). The thermal conductivity was implemented with the samples with dimensions of φ 39 × 15 mm by using a Hot Disk TPS2500 apparatus with a 5465 sensor. The thermal insulation effect of PIA-O_2B_2, PIA-O_3B_3, and PIA-O_4B_4 was tested by the self-assembled experimental apparatus (including a thermostat water bath (DF-101S) and infrared thermal imager (Fluke Tis 60+) with Sony camera recorder (α7 II)). The self-extinguishing properties of PIA-O_2B_2, PIA-O_3B_3, and PIA-O_4B_4 were tested with a blowtorch flame. The hydrophobicity of PIA-O_2B_2 was characterized using the contact angle tester (SZ-CAM). Water uptake of PIA-O_2B_2 after hydrophobic treatment was tested using HT8–100. The compressive tests were carried out on a microcomputer electronic universal testing machine (XBD4204). The top platen was allowed to fall at a speed of 0.5 mm min^{-1}, and the bottom one was immovable. PIA-O_2B_2, PIA-O_3B_3, and PIA-O_4B_4 were analyzed for thermal properties using thermogravimetry and differential scanning calorimetry. The test temperature range was from room temperature to 700 °C at a rate of 5 °C min^{-1} in air atmosphere.

3. RESULTS AND DISCUSSION

3.1. Pore Structure. Figure 2 shows the microscopic morphologies of PIA-O_2B_2, PIA-O_3B_3, and PIA-O_4B_4, which comprehensively exhibit a representative three-dimensional networking structure with a gradually enlarging view. As a whole, the morphological structures of all of the above are comprised of pearl-necklace-like skeletons, presenting the formation of the interpenetrating networking. The networking structure entangles randomly to give a porous architecture. PIA-O_2B_2 exhibits an open-cellular structure, where the mesopores account for the majority of the pores. Compared to the other groups, PIA-O_2B_2 possesses small and dense pores at the nanoscale, which results in the low thermal conductivity because of the pore size being smaller than the mean free path of static air at room temperature. The networking structure impedes the motion of polyimide molecular chains during the gelation process and reduces the shrinkage of the gel to some

https://doi.org/10.1021/acsapm.2c01180
ACS Appl. Polym. Mater. 2022, 4, 8227–8237

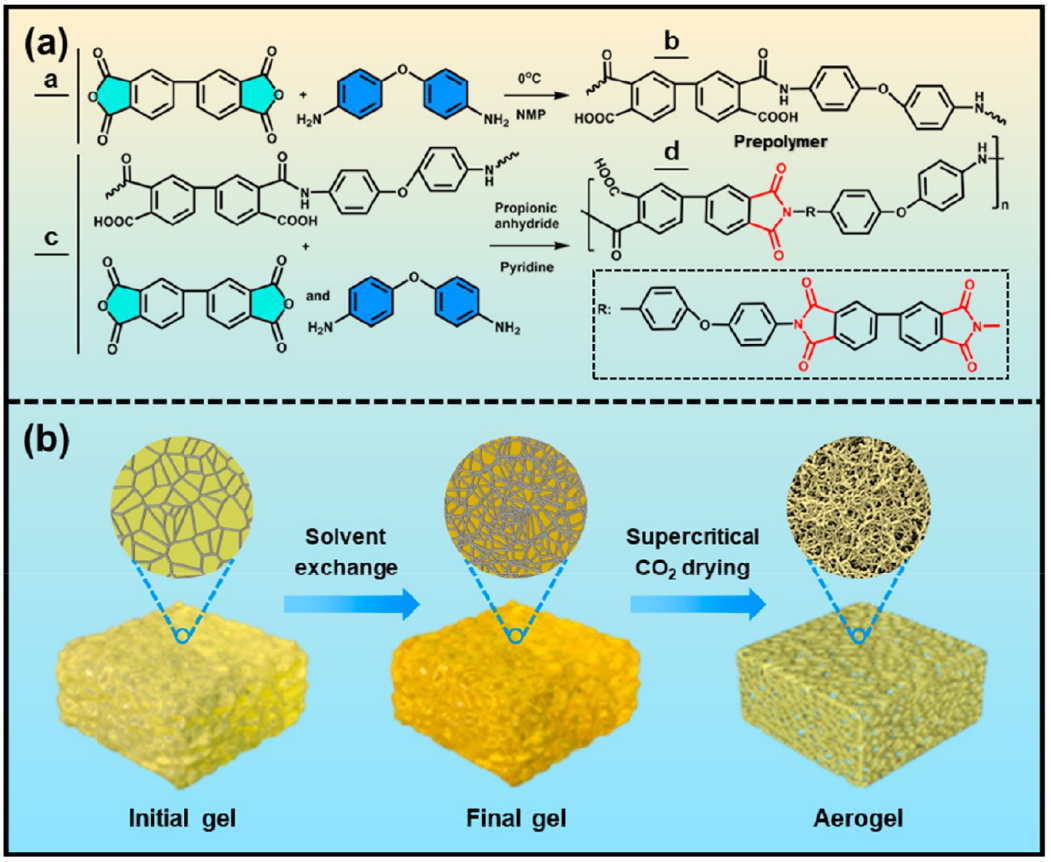

Figure 3. Chemical reaction mechanism and preparation diagram of PIA series. (a) Chemical reaction mechanism and (b) fabrication diagram.

extent. The drying shrinkage rate of PIA-O_2B_2 is 2.31%, which is lower than PIA-O_3B_3 and PIA-O_4B_4 in Figure 1l. The reason is that the amino and carboxyl groups in the introduced prepolymer molecular chain can form chemical bonds with ODA and BPDA monomers by the condensation reaction, which can increase the polymerization of the system. Thus, the introduction of prepolymers not only achieves the similar effect to physical chain entanglement but also allows for structural enhancement by increasing the degree of the reaction. Based on FESEM monitoring of the polyimide aerogel skeleton structure, reinforced polyimide aerogels by prepolymers are homogeneous and have a well-defined networking skeleton structure, achieving reinforcement of the polyimide aerogel skeleton. The structural enhancement will largely help to suppress the shrinkage of the polyimide aerogels before and after drying in supercritical fluids. In other words, FESEM data not only are quite consistent with the results from BET tests but also demonstrate the structure−property relation of PIA from the design synthesis perspective.

The N_2 adsorption−desorption isotherms of PIA-O_2B_2, PIA-O_3B_3, and PIA-O_4B_4 were measured with the hysteresis at a limited pressure in Figure S2a−c, which are typical IV-type curves according to IUPAC. The isotherms of PIA series with a hysteresis loop at high relative pressure were observed, indicating the presence of mesopores in the aerogels. When the ratio of P/P_0 is controlled to within 0.0−0.1, the adsorption capacity is minimal. This phenomenon indicates that there are few micropores in PIA. The adsorption capacity gradually increases during a P/P_0 range of 0.2−0.7, and the nonlinear increasing nitrogen uptake is observed from 0.8 to 1.0 based on P/P_0, owing to the presence of multilayer adsorption in a relative high pressure. This case indicates that there are mesopores and macropores of PIA. The pore size and its distribution are clearly given from Figure S2d−f to further make sure of the porous texture of PIA using BJH theory. The pore sizes of the PIA series are mainly in the range of 2−60 nm, which is in accordance with the pore architecture features revealed by the adsorption−desorption isotherms. Besides this, the focusing degree of PIA-O_2B_2 is superior to the other ones, suggesting PIA with porous interior and mesopores. This result is generally consistent with the results from FESEM images (Figure 2).

3.2. Cross-Linking Reaction. The drying shrinkage of PIA series has been dramatically improved due to its skeleton enhancement. How exactly is this network structure formed? At the beginning of the reaction, the prepolymer starts to react to form the prepolymer polyamide acid linear networking structure. Afterward, the prepolymer molecular chains undergo partial condensation reactions, hydrogen bonding, and physical entanglement between the chains with the added ODA and BPDA monomers under the catalysis of propionic anhydride and pyridine in Figure 3a, which are less likely to be entangled and crossed due to the slow movement of the molecular chains at low temperature. As the temperature increases and the aging and solvent exchange process proceeds, the thermal movement of the molecular chains accelerates and the reaction becomes more adequate. The behavior results in the rapid growth and enhancement of the skeletal structure, which is more easily entangled and crossed between chains to form the strong nanoporous cross-linked networking structure. The pearl-necklace-like three-dimensional nanoporous structure of PIA is obtained by supercritical drying and solvent removal in

https://doi.org/10.1021/acsapm.2c01180
ACS Appl. Polym. Mater. 2022, 4, 8227−8237

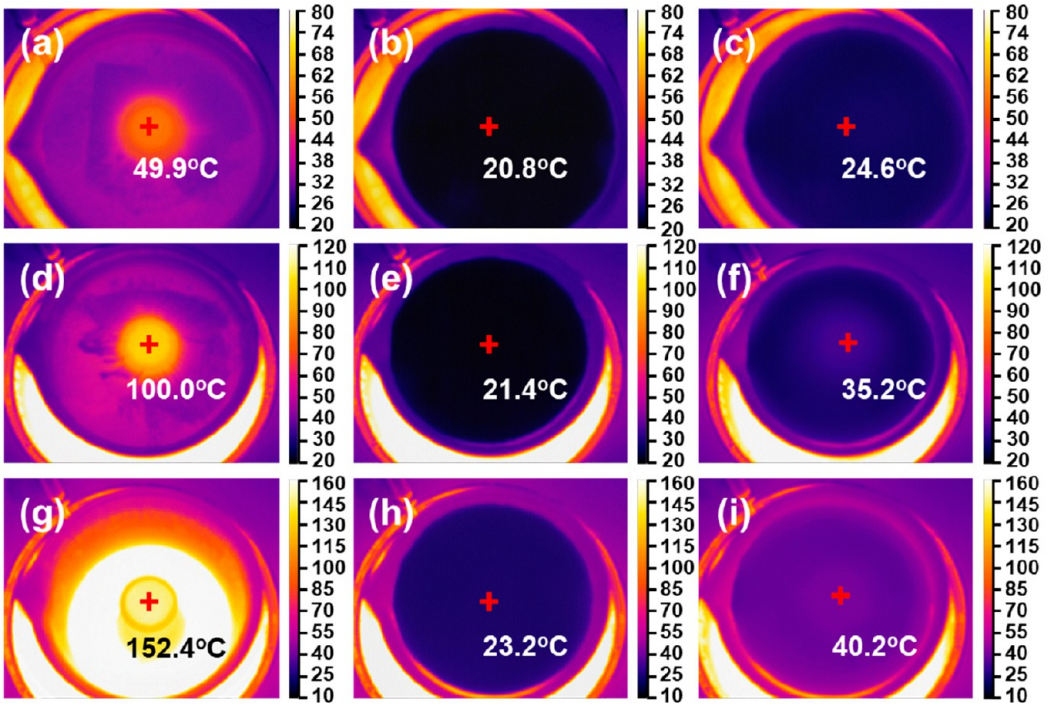

Figure 4. Temperature changes monitored at the center of the cold surface of PIA-O_2B_2 on heating plates of 50, 100, and 150 °C for 30 min. The cases for the related hot surfaces with the temperatures of PIA-O_2B_2 at (a–c) 50 °C, (d–f) 100 °C, and (g–i) 150 °C, respectively.

Figure 3b. In the supercritical drying method, liquid in the gels is transformed into gas, which is commonly used to convert the final gels into aerogels. Herein, the nanoporous networking structure is sustained due to the lack of involvement of capillary stress and surface tension. This process has the capability to remove liquid from wet gels with the least damage to them and form highly porous and more uniform pore structure than the freeze-drying technique.[24]

To verify the successful synthesis of the PIA, FTIR and XPS experiments were systematically conducted. Figure S3a shows the peaks at 741, 1370, 1500, and 1720 cm^{-1}, confirming the presence of the imide functional group. The absorption bands at 1720, 1370, and 741 cm^{-1} correspond to the symmetrical stretching of the C═O group, stretching of the C–N in the imide rings and bending of the C═O group.[25] The absence of strong peaks at 1620 and 3000 cm^{-1} indicate that the majority of polyamide acid is imidized. The absorbance peak at 1500 cm^{-1} corresponds to the benzene ring, signifying the formation of chains comprised of benzene ring structure. According to the above results, the formation of polyimide absorption peaks is proved, indicating the existence of imide structure in the PIA.

The XPS spectra in Figure S3b display the characteristic peaks of PIA-O_2B_2 centered at 288.08 (C 1s), 400.08 (N 1s), and 531.48 eV (O 1s), indicating the successful synthesis of polyimide. For further analysis, the peaks detected at binding energies of 284.68 and 288.08 eV (C 1s) of PIA originate from C–C and C═O, respectively (Figure S4a). The presence of C═O bond can be attributed to the anhydride group of 3,3′,4,4′-biphenyltetracarboxylicdianhydride, demonstrating the reaction of BPDA and ODA. The emerging peak of –CO–N–CO– at 531.48 eV is ascribed to imide groups in Figure S4c, which is consistent with FTIR. The formation of the bond can be well attributed to reaction between –CONH and –COOH groups. As a reference, the XPS information on PIA-O_3B_3 and PIA-O_4B_4 have been also provided in Figure S3c,d, wherein C 1s, N 1s, and O 1s data are generally conformed to those of PIA-O_2B_2, stating clearly the existence of main chemical bonds in forming networking structures.

3.3. Thermal Insulation Evaluation. The temperature variations of PIA-O_2B_2 (Figure 4) throughout the thermal insulation test was recorded by an infrared thermal imager. In the initial stage, the central temperatures of the conical flask were controlled at 50, 100, and 150 °C before measurement of PIA-O_2B_2 (Figure 4, parts a, d, and g), respectively. The first column shows the actual temperatures, which are 49.9, 100, and 152.4 °C, respectively. After placing PIA-O_2B_2, the initial temperatures of the cold surface are detected to be 20.8, 21.4, and 23.2 °C (Figure 4, parts b, e, and h), respectively, and the temperatures of the cold surface increase with time. With time extending (total time: 30 min), the temperatures on the cold surface are 24.6, 35.2, and 40.2 °C, respectively (Figure 4, parts c, f, and i). As the temperature of the hot surface increases, the thermal insulation property is more outstanding according to the data concerning the temperature changes of the cold surface. Under the high-temperature conditions, the thermal insulation performance is best, thanks to the uniform pore structure. The stabilized cold surface temperatures of PIA-O_3B_3 are 34.3, 48.3, and 57.4 °C, respectively, while the temperatures of PIA-O_4B_4 are 34.1, 50.5, and 59.7 °C, respectively, in Figure S5.

Compared with PIA-O_3B_3 and PIA-O_4B_4, PIA-O_2B_2 shows the better thermal insulation effect. The superior insulation performance of PIA-O_2B_2 is mainly attributed to the relatively symmetrical pore structure, which can be clearly seen from the FESEM data in Figure 2. Due to the existence of nearly infinite number of nanopore, heat flow in the solid structure of aerogel material can only be transmitted along the stomatal wall and the infinite number of stomatal walls constitute the infinite long path, resulting in the lowest temperatures of PIA-O_2B_2

https://doi.org/10.1021/acsapm.2c01180
ACS Appl. Polym. Mater. 2022, 4, 8227–8237

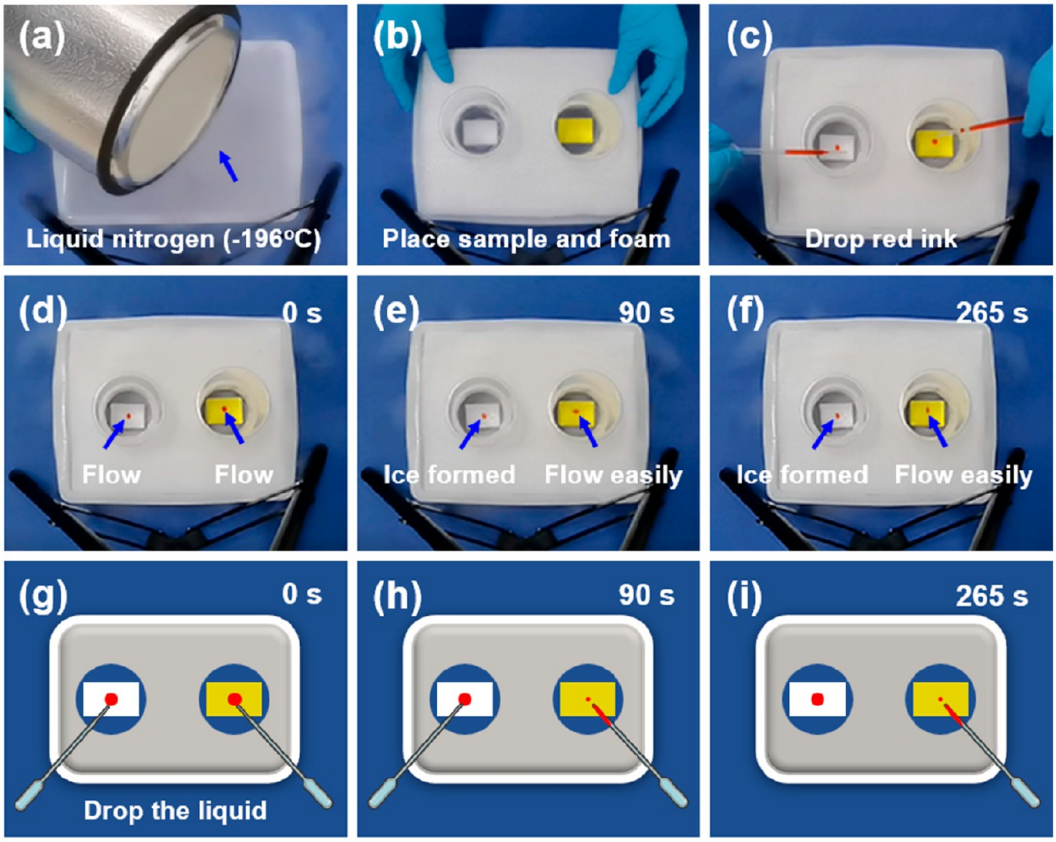

Figure 5. Photographs of thermal insulation properties of PIA-O_2B_2 in the low-temperature environment of −196 °C (compared with the foam). (a) Pouring liquid nitrogen into plastic containers, (b) placing the sample and foam (foam on the left, sample on the right), (c) dropping red ink, (d) the state of the liquid, (e) the liquid on the foam freezes and the droplet on the sample remains the liquid shape for 90 s, (f) the droplet on the sample remains the near-spherical shape for 265 s, and (g−i) corresponding schematic diagrams of the state of the liquid.

after the hot flow balance. Thermal conductivity test is conducted to further clarify the reason for good thermal insulating property and the optimal value is 0.0238 W m^{-1} K^{-1} (Figure 1j). PIA-O_2B_2 shows the lowest thermal conductivity, because the smaller pore size and continuous three-dimension porous structure can effectively restrain gaseous thermal transfer and slow the thermal transfer rate.

In addition to testing high-temperature environment, the cryogenic environment is also a key part for the examination of thermal insulation materials in deep exploration. As PIA-O_2B_2 exhibits good thermal insulation performance under high-temperature conditions, then how well does its thermal insulation performance do under cryogenic conditions? Photos of different stages are taken from the video to show the thermal insulation performance of PIA-O_2B_2 under cryogenic conditions in Figure 5 and Video S1. Specifically, the liquid nitrogen was gradually dumped into the vessel and the plastic cups containing the foam and PIA-O_2B_2 were laid in the liquid nitrogen (−196 °C). Red ink was dropped onto the surface of the foam and PIA-O_2B_2 at the same time, and the time was recorded. The ink on the foam surface was frozen, while the ink on the PIA-O_2B_2 was still fluid at 90 s. The liquid on PIA-O_2B_2 can still flow as long as 265 s later, which proves that PIA-O_2B_2 still has excellent thermal insulation performance under cryogenic conditions. As demonstrated by FESEM and BET, PIA-O_2B_2 with the homogeneous pore structure and small pores size have superior thermal insulation performance in cryogenic environment. The corresponding schematic diagrams are drawn to better show the process of liquid solidifying. PIA-O_2B_2 gives excellent thermal insulation performance under cryogenic atmosphere, suggesting the potential of practical applications in a cryogenic environment.

3.4. Self-Extinguishing Feature and Hydrophobic Property. A series of PIAs were processed into cubes in size of 1 cm × 1 cm × 1 cm and tested by burning the corresponding samples with a blowtorch (external flame temperature: approximately 1200 °C) to evaluate the self-extinguishing property of PIA-O_2B_2, PIA-O_3B_3, and PIA-O_4B_4. Photos of three stages were taken from the video to show the self-extinguishing property of PIA-O_2B_2, PIA-O_3B_3, and PIA-O_4B_4. The combustion process of PIA series is depicted and the experimental video is available in the Supporting Information (see Figure S6 and Video S2). The PIA series burned slowly by touching the outer flame and self-extinguished after moving away from it for a period of time. The presence of aromatic ring in the diamine and dianhydride monomers improves heat resistance and increases the degree of charring by changing the molecular structure through the cyclization reaction, so that the flame goes out after removal of the fire source. In the same burning time, PIA-O_2B_2 is extinguished in 0.08 s after leaving the flame, which proves that PIA-O_2B_2 has better flame-retardant performance than PIA-O_3B_3 (0.10 s) and PIA-O_4B_4 (0.09 s).

The hydrophilicity of PIA is due to the hydrogen bonding and van der Waals forces of polar groups (−COOH, −CONH, C═O), which can lead to material failure during the

https://doi.org/10.1021/acsapm.2c01180
ACS Appl. Polym. Mater. 2022, 4, 8227−8237

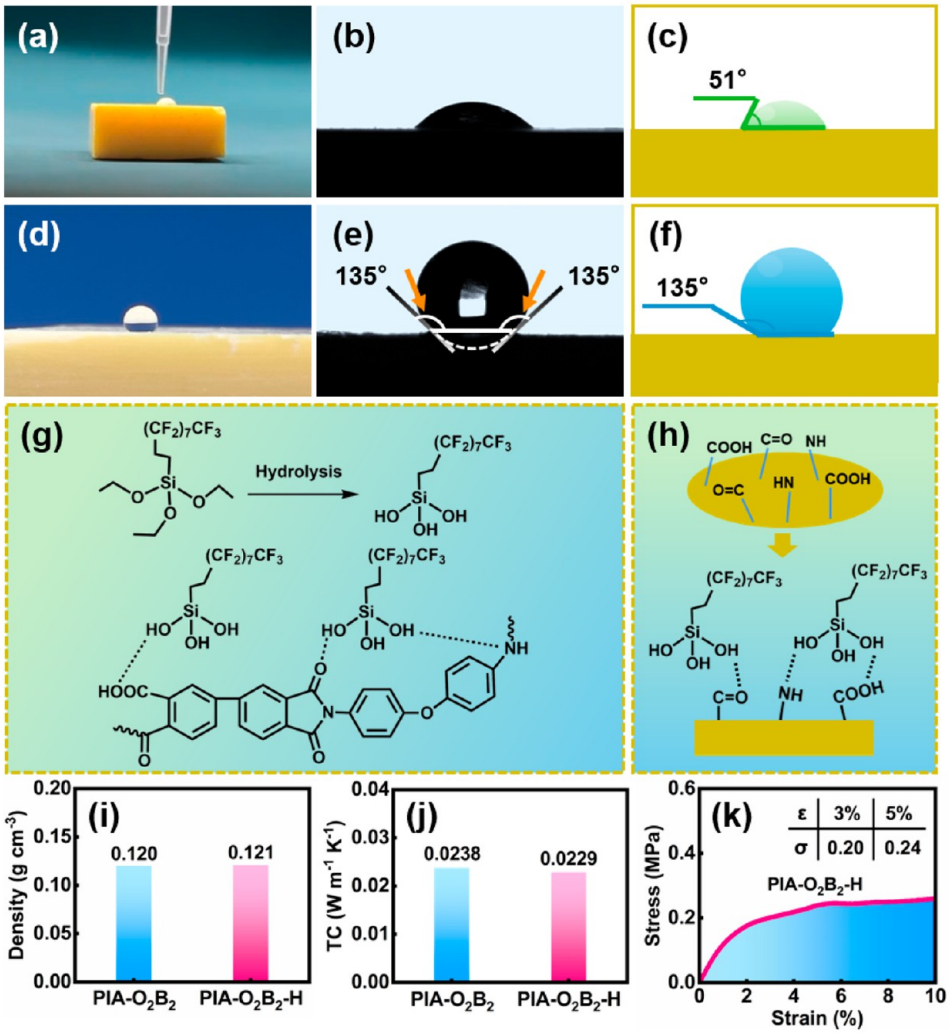

Figure 6. Photos before and after hydrophobic treatment, hydrophobic mechanism and the properties of PIA-O_2B_2. (a−c) The cases for droplet on the hydrophilic sample, the water contact angle, and corresponding schematic of hydrophilic sample, (d−f) the cases for droplet on the hydrophobic sample, the water contact angle and corresponding schematic of hydrophobic sample, (g, h) hydrophobic mechanism, (i, j) density and thermal conductivity of PIA-O_2B_2 and hydrophobic-treated PIA-O_2B_2 (PIA-O_2B_2-H) and (k) the compressive stress−strain curve of PIA-O_2B_2-H.

return of the vehicle to the ground. The water droplet is absorbed and begins to spread around on the surface of hydrophilic PIA-O_2B_2, and the water contact angle of PIA-O_2B_2 is 51° in Figure 6a−c. However, the water droplet is difficult to wet on the surface of PIA-O_2B_2 after hydrophobic treatment and the water contact angle of PIA-O_2B_2 could reach up to 135° (Figure 6d−f), implying a greater advantage than for the intrinsic aerogels. The hydrophobic mechanism is proposed to explain hydrophobicity in Figure 6g. The hydrophobic agent PFDTES is fully hydrolyzed by adding deionized water and stirring appropriately, and the fully hydrolyzed PFDTES is placed under the shelf with PIA-O_2B_2. PIA-O_2B_2 is imparted hydrophobicity by grafting hydrolyzed PFDTES onto its surface via hydrogen bonding using chemical vapor deposition at 75 °C in Figure 6h. PIA-O_2B_2 has excellent hydrophobicity due to the introduction of the large amount of fluorine groups. The water droplets can slip on the surface of PIA-O_2B_2 (Video S3), and this lotus effect prevents the structure of PIA-O_2B_2 from being damaged by water. In addition, the hydrophobic treated PIA-O_2B_2 (PIA-O_2B_2-H) were tested for the density, thermal conductivity and mechanical property to determine whether the hydrophobic treatment had any effect on the performance of PIA-O_2B_2 in Figure 6i−k. The density of PIA-O_2B_2 has a slight but negligible change after hydrophobic treatment due to the introduction of PFDTES. Compared with PIA-O_2B_2, the low thermal conductivity of PIA-O_2B_2-H is attributed to the attachment of PFDTES to the skeleton of PIA-O_2B_2, which makes the original macropore smaller, reducing the thermal conductivity. In the linear growth stage, the introduction of PFDTES has no effect on the mechanical property, but the effect on the mechanical properties gradually appears with the increase of the strain. The reason for the deterioration of mechanical property may be that the attachment of PFDTES has the effect of similar point defects on the PIA-O_2B_2 skeleton. Moreover, the mass water uptake rate of PIA-O_2B_2-H is 3.7% under the conditions of 50 °C and 95% humidity for 5 h.

3.5. Mechanical and Processability. The mechanical characteristics including toughness and robustness need to be soundly matched to the requisites for practical application in the aerospace field. The compressive stress−strain curves of

https://doi.org/10.1021/acsapm.2c01180
ACS Appl. Polym. Mater. 2022, 4, 8227−8237

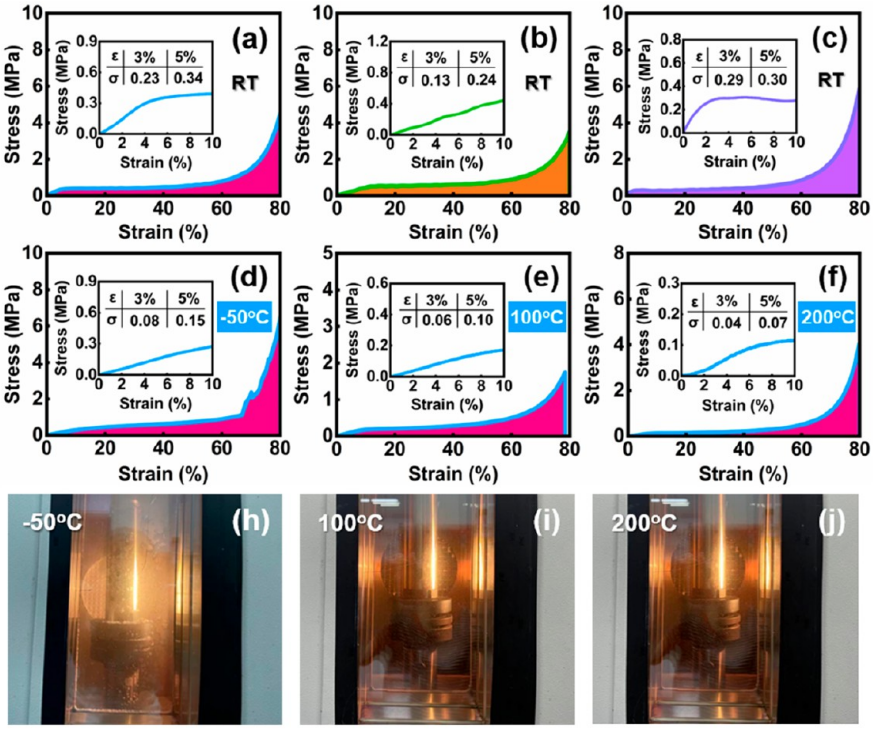

Figure 7. Compressive stress−strain curves of PIA series. (a−c) Compressive stress−strain curves of PIA-O_2B_2, PIA-O_3B_3, and PIA-O_4B_4 at room temperature, (d−f) compressive stress−strain curves of PIA-O_2B_2 at −50, 100, and 200 °C, respectively, and (h−j) compressive process pictures of PIA-O_2B_2 at −50, 100, and 200 °C, respectively.

PIA series at room temperature are given in Figure 7a−c, which are similar to those of the previous PIA and other polymer reinforced aerogels. In the range of initial compression, PIA-O_2B_2, PIA-O_3B_3, and PIA-O_4B_4 show a linear relationship with compressive stress−strain at the low strain of 3−10%, and the deformation is reversible. The nonreversible deformation of PIA series takes place, where the skeleton starts to collapse and the pores are extruded into smaller pores or thoroughly broken with the strain increasing in the range of 10−60%. The compressive stress of PIA series increases dramatically and the materials become dense relative to the original, reflecting an abrupt slope on the stress−strain curves when the strain exceeds 60%. Compared with PIA-O_3B_3 and PIA-O_4B_4, PIA-O_2B_2 exhibits the better mechanical properties (3% strain corresponding to the stress: 0.23 MPa) because of abundant and uniform pores inside PIA-O_2B_2.

The optimal PIA-O_2B_2 is tested for temperature resistance, including high temperature and low temperature (−50, 100, and 200 °C) in Figure 7d−j. Generally, most polymeric materials become hard and brittle at −50 °C, but the mechanical properties of PIA-O_2B_2 only become worse and the material is not brittle at the low temperature. The reason for this phenomenon is explained from the perspective of molecular motion that the mitigation of molecular chain thermal motion, the reduction of molecular chain flexibility and the shortening of the intermolecular distance leads to cracks or even fractures in the skeleton of polyimide aerogel at low temperature. The macroscopic manifestation is the degradation of mechanical properties at low temperature. Although the mechanical properties have degraded, it can still meet the demand of thermal protection materials for aircraft at low temperature mainly due to the strengthening of polyimide aerogel framework. These results suggest that PIA-O_2B_2 can maintain mechanical performances well under low temperature condition and be also served even at 200 °C.

The processability of PIA is of great significance to its practical application. PIA-O_2B_2 is tested for compression resistance to better demonstrate the good mechanical properties of PIA series. As can be seen in Figure 8a, the excellent

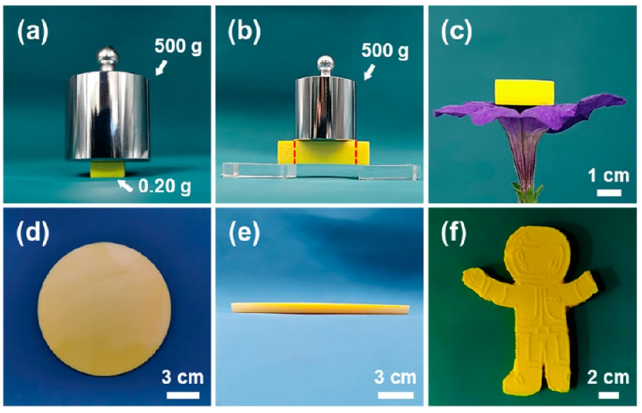

Figure 8. Pictures for reflecting mechanical and processability properties of PIA-O_2B_2. (a) The presentation of compressive strength, (b) the presentation of supporting ability, (c) the lightweight and low density, and (d−f) the presentation of processability.

mechanical strength of PIA-O_2B_2 has been proved to be able to carry heavy objects of 2500 times its weight without structural damage, which is identical with the compressive stress−strain curves. As represented in Figure 8b, the good supporting strength of PIA-O_2B_2 attributed to its strong skeleton structure is demonstrated by lapping PIA-O_2B_2 between glass sheets and placing a 500 g weight on the PIA-O_2B_2, which remains its

https://doi.org/10.1021/acsapm.2c01180
ACS Appl. Polym. Mater. 2022, 4, 8227−8237

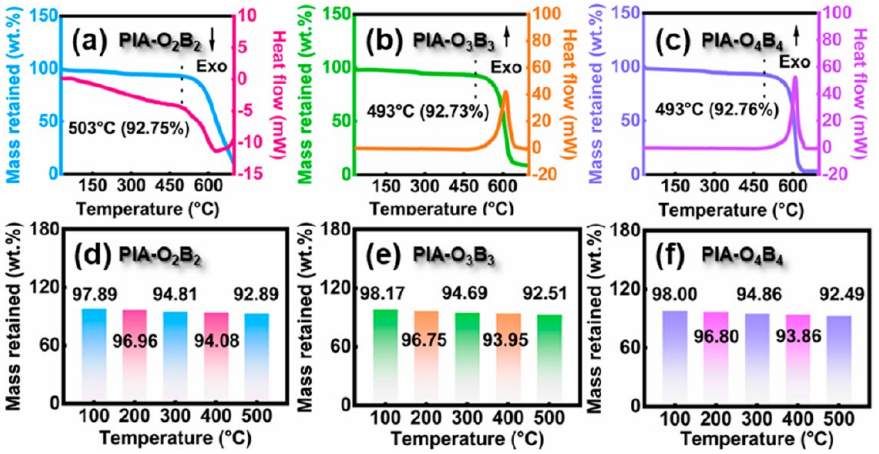

Figure 9. TG-DSC curves and residual rates at different temperatures under air atmosphere of PIA series. (a, d) PIA-O_2B_2, (b, e) PIA-O_3B_3, and (c, f) PIA-O_4B_4.

original state without visible cracks on the surface of PIA-O_2B_2. In addition, the flower could bear the obtained PIA-O_2B_2 without deformation in Figure 8c, which shows the lightweight merit of PIA, and the density of 0.12 g cm^{-3} is shown in Figure 1k. What is even more interesting is that PIA series can be processed into different shapes, such as cylinder, cubes, and a profile-shaped structure. Parts d and e of Figure 8 provide the main view and top view of the cylinder of PIA series whose surface is flat and smooth. The PIA series is easy to process and can be machined into a profile-shaped structure as demonstrated by observing the tiny texture on the surface of the astronaut shaped sample in Figure 8f. The excellent processability and mechanical properties of PIA series provide convenience for their applications in the field of thermal insulation in aerospace.

3.6. Thermal Stability and Dimensional Stability. High thermal stability of PIA plays an important role in manufacturing thermal insulation materials in aerospace. TG and DSC curves are conducted to evaluate the thermal stability of PIA-O_2B_2, PIA-O_3B_3, and PIA-O_4B_4 from room temperature to 700 °C under air atmosphere. The small weight loss is due to adsorbed water, free water, and NMP decomposition, which appears within 25−300 °C at the initial stage. The loss in weight occurring after 500 °C is due to weak bond fracture and continuous thermal decomposition of PIA-O_2B_2, PIA-O_3B_3, and PIA-O_4B_4. Furthermore, the obvious endothermic peaks of PIA series are discovered about 600 °C as illustrated the DSC curves in Figure 9a−c, which are primarily attributed to the thermal decomposition process of PIA series and other thermal behaviors. As seen in Figure 9, maximum decomposition rate temperatures (T_{max}) of PIA-O_3B_3 and PIA-O_4B_4 are identified to be 493 and 493 °C, which are lower than PIA-O_2B_2 (T_{max} = 503 °C). The degradation of the thermal stability is mainly ascribed to the increased content of the flexible groups (C−O−C) of PIA-O_3B_3 and PIA-O_4B_4, inducing the decomposition of PIA-O_3B_3 and PIA-O_4B_4 at the lower temperatures. In addition, PIA-O_2B_2 has the higher percentage of residual weight despite experiencing the programmed heating process of 700 °C, which may be due to the high content of networking skeletons derived from the chains containing aromatic structure in PIA-O_2B_2. The residual rates of PIA-O_2B_2, PIA-O_3B_3, and PIA-O_4B_4 are also listed to accurately evaluate the thermal decomposition process from 100 to 500 °C in Figure 9d−f. The residual rates of PIA-O_2B_2 are relatively higher than those of PIA-O_3B_3 and PIA-O_4B_4 within 100−500 °C, fully demonstrating better thermal stability.

Dimensional stability is another crucial factor for practical applications of PIA in aircraft. PIA-O_2B_2 is selected as the optimal group to test dimensional stability based on the above suitable pore structure, excellent thermal insulation performance, and low thermal conductivity experimental results. To visually assess the dimensional stability of PIA at high temperature (200 °C), the thermal treatment is carried out under high-temperature conditions (Figure 10). Before the

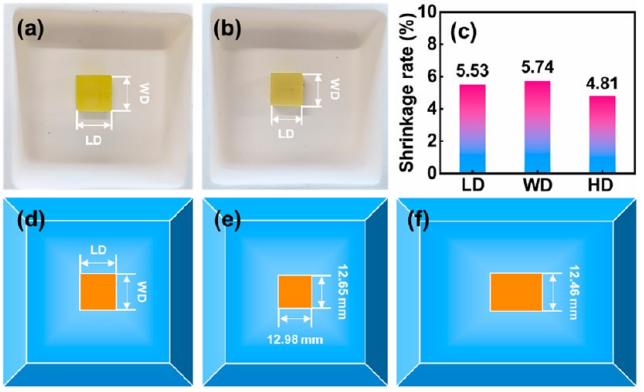

Figure 10. Dimensional changes of PIA-O_2B_2 at 200 °C for 10 min. (a, d) Before the thermal treatment, (b, e, f) after the thermal treatment, and (c) shrinkage rates of length direction (LD), width direction (WD), and height direction (HD).

thermal treatment, PIA-O_2B_2 is processed into cube (size: 13.74 mm × 13.40 mm × 13.09 mm), and the corresponding dimensions are also collected for calculating shrinkage changes along the uniaxial direction after the thermal treatment. The size changes of PIA-O_2B_2 are showed at 200 °C, whose shrinkage after thermal treatment shows a little difference. The shrinkage rates of LD, WD and HD are 5.53, 5.74 and 4.81%, respectively, and the shrinkage along the uniaxial direction is substantially inhibited compared with other literatures (20%)[26,27] because the free volume of molecular chain is small.

4. CONCLUSIONS

In summary, PIAs with the typical mesoporous structure have been fabricated successfully by two-step prepolymerization and

https://doi.org/10.1021/acsapm.2c01180
ACS Appl. Polym. Mater. 2022, 4, 8227−8237

a polycondensation method. The obtained PIA-O_2B_2 demonstrate low drying shrinkage (2.31%), low thermal conductivity (0.0238 W m^{-1} K^{-1}), superior thermal insulation in the wide temperature window (−196−150 °C), exceptional flame-retardant properties (extinguish in 0.08 s after leaving the flame), hydrophobic property (water contact angle: 135°), moderate mechanical properties (3% strain corresponding to the stress: 0.23 MPa), outstanding processability, good thermal stability (decomposition temperature: 503 °C), and low high temperature shrinkage (4.81%). The results suggest that PIA-O_2B_2 could be an excellent thermal insulation material in extreme conditions, which might be applied in batteries, fire resistance, and other fields. We expect that our work will motivate research efforts on the production of PIA, realizing a broad range of practical applications in thermal protection systems, reducers, aircraft antenna, and other aerospace fields in the future.

■ ASSOCIATED CONTENT

Supporting Information

The Supporting Information is available free of charge at https://pubs.acs.org/doi/10.1021/acsapm.2c01180.

Video S1: Thermally insulating test of PIA-O_2B_2 at cryogenic environment (ZIP)

Video S2: Self-extinguishing test of PIA-O_2B_2 (ZIP)

Video S3: Hydrophobic test of PIA-O_2B_2 (ZIP)

Images for samples (gels and aerogels) of PIA-O_1B_1, PIA-O_xB_x (x = 5, 6, or 7) and PIA-O_8B_8; N_2 adsorption−desorption isotherms and pore distribution of PIA-O_2B_2, PIA-O_3B_3, and PIA-O_4B_4; FTIR and XPS spectra of PIA-O_2B_2, PIA-O_3B_3, and PIA-O_4B_4; C 1s, N 1s, and O 1s spectra of PIA-O_2B_2, PIA-O_3B_3, and PIA-O_4B_4 depending on XPS; temperature changes monitored at the center of the cold surface of PIA-O_3B_3 and PIA-O_4B_4; and self-extinguishing tests of PIA-O_2B_2, PIA-O_3B_3, and PIA-O_4B_4 before, during, and after combustion (PDF)

■ AUTHOR INFORMATION

Corresponding Author

Sizhao Zhang − *Polymer Aerogels Research Center, Jiangxi University of Science and Technology, Ganzhou 341000 Jiangxi, China; Postdoctoral Research Station on Mechanics, College of Aerospace Science and Engineering, National University of Defense Technology, Changsha 410073 Hunan, China;* orcid.org/0000-0003-2321-5138; Email: zhangsz@jxust.edu.cn

Authors

Zhao Wang − *Polymer Aerogels Research Center, Jiangxi University of Science and Technology, Ganzhou 341000 Jiangxi, China*

Jing Wang − *Polymer Aerogels Research Center, Jiangxi University of Science and Technology, Ganzhou 341000 Jiangxi, China*

Yunyun Xiao − *Polymer Aerogels Research Center, Jiangxi University of Science and Technology, Ganzhou 341000 Jiangxi, China*

Zhouyuan Yang − *Polymer Aerogels Research Center, Jiangxi University of Science and Technology, Ganzhou 341000 Jiangxi, China*

Hui Ji − *Polymer Aerogels Research Center, Jiangxi University of Science and Technology, Ganzhou 341000 Jiangxi, China*

Guangyu Xu − *Polymer Aerogels Research Center, Jiangxi University of Science and Technology, Ganzhou 341000 Jiangxi, China*

Shixian Xiong − *Polymer Aerogels Research Center, Jiangxi University of Science and Technology, Ganzhou 341000 Jiangxi, China*

Zhengquan Li − *Polymer Aerogels Research Center, Jiangxi University of Science and Technology, Ganzhou 341000 Jiangxi, China;* orcid.org/0000-0002-7890-7257

Feng Ding − *Polymer Aerogels Research Center, Jiangxi University of Science and Technology, Ganzhou 341000 Jiangxi, China*

Complete contact information is available at: https://pubs.acs.org/10.1021/acsapm.2c01180

Notes

The authors declare no competing financial interest.

■ ACKNOWLEDGMENTS

The authors greatly express thanks for the financial support from the General Project of Jiangxi Provincial Key Research and Development Program (Grant No. 20212BBG73001), the Jiangxi Provincial Natural Science Foundation (Grant No. 20202BABL214014), the Project funded by China Postdoctoral Science Foundation (Grant No. 2021M693969), the General Project of Ganzhou Municipal Key Research and Development Program (Grant No. 202101124914), and the Industry Field Project of Ganzhou Municipal Key Research and Development Program.

■ REFERENCES

(1) Li, X.; Dong, G.; Liu, Z.; Zhang, X. Polyimide Aerogel Fibers with Superior Flame Resistance, Strength, Hydrophobicity, and Flexibility Made via a Universal Sol-Gel Confined Transition Strategy. *ACS Nano* **2021**, *15* (3), 4759−4768.

(2) Su, K.; Wang, Y.; Hu, K.; Fang, X.; Yao, J.; Li, Q.; Yang, J. Ultralight and High-Strength SiC_{nw}@SiC Foam with Highly Efficient Microwave Absorption and Heat Insulation Properties. *ACS Appl. Mater. Interfaces.* **2021**, *13* (18), 22017−22030.

(3) Zhu, J.; Zhao, F.; Peng, T.; Liu, H.; Xie, L.; Jiang, C. Highly Elastic and Robust Hydroxyapatite Nanowires/Polyimide Composite Aerogel with Anisotropic Structure for Thermal Insulation. *Composites Part B-Engineering.* **2021**, *223*, 109081.

(4) Issaoui, H.; de Hoyos-Martinez, P. L.; Pellerin, V.; Dourges, M.-A.; Deleuze, H.; Bourbigo, S.; Charrier-El Bouhtoury, F. Effect of Catalysts and Curing Temperature on the Properties of Biosourced Phenolic Foams. *ACS Sustainable Chemistry Engineering.* **2021**, *9* (18), 6209−6223.

(5) Shi, D.; Teng, X.; Jing, X.; Lyu, S.; Yang, X. A Multi-scale Stochastic Model for Damage Analysis and Performance Dispersion Study of A 2.5 D Fiber-reinforced Ceramic Matrix Composites. *Composite Structures.* **2020**, *248*, 112549.

(6) Li, L. A Micromechanical Temperature-dependent Vibration Damping Model of Fiber-reinforced Ceramic-matrix Composites. *Composite Structures.* **2021**, *261*, 113297.

(7) Tong, Y.; Hu, Y.; Liang, X.; Zhang, Z.; Li, Y.; Chen, Z.; Xiong, X.; Hua, M. Carbon Fiber Reinforced ZrC Based Ultra-High Temperature Ceramic Matrix Composite Subjected to Laser Ablation: Ablation Resistance, Microstructure and Damage Mechanism. *Ceram. Int.* **2020**, *46* (10), 14408−14415.

(8) Zhang, S.; He, J.; Xiong, S.; Xiao, Q.; Xiao, Y.; Ding, F.; Ji, H.; Yang, Z.; Li, Z. Construction and Nanostructure of Chitosan/

Nanocellulose Hybrid Aerogels. *Biomacromolecules.* **2021**, *22* (8), 3216−3222.
(9) Xiong, S.; Yang, Y.; Zhang, S.; Xiao, Y.; Ji, H.; Yang, Z.; Ding, F. Nanoporous Polybenzoxazine Aerogels for Thermally Insulating and Self-extinguishing Materials in Aerospace Applications. *ACS Appl. Nano Mater.*. **2021**, *4* (7), 7280−7288.
(10) Li, M.; Gan, F.; Dong, J.; Fang, Y.; Zhao, X.; Zhang, Q. Facile Preparation of Continuous and Porous Polyimide Aerogel Fibers for Multifunctional Applications. *ACS Appl. Mater. Interfaces.* **2021**, *13* (8), 10416−10427.
(11) Xue, T.; Fan, W.; Zhang, X.; Zhao, X.; Yang, F.; Liu, T. Layered Double Hydroxide/Graphene Oxide Synergistically Enhanced Polyimide Aerogels for Thermal Insulation and Fire-retardancy. *Composites Part B-Engineering.* **2021**, *219*, 108963.
(12) Liu, H.; Chen, X.; Zheng, Y.; Zhang, D.; Zhao, Y.; Wang, C.; Pan, C.; Liu, C.; Shen, C. Lightweight, Superelastic, and Hydrophobic Polyimide Nanofiber/MXene Composite Aerogel for Wearable Piezoresistive Sensor and Oil/Water Separation Applications. *Advanced Functional Materials.* **2021**, *31* (13), 2008006.
(13) Jiang, S.; Uch, B.; Agarwal, S.; Greiner, A. Ultralight, Thermally Insulating, Compressible Polyimide Fiber Assembled Sponges. *ACS Appl. Mater. Interfaces.* **2017**, *9* (37), 32308−32315.
(14) Zhang, T.; Zhao, Y.; Muhetaer, M.; Wang, K. Silver Nanoparticles Cross-linked Polyimide Aerogels with Improved High Temperature Microstructure Stabilities and High Mechanical Performances. *Microporous Mesoporous Mater.* **2020**, *297*, 110035.
(15) Zhao, Z.; Cui, Y.; Kong, Y.; Ren, J.; Jiang, X.; Yan, W.; Li, M.; Tang, J.; Liu, X.; Shen, X. Thermal and Mechanical Performances of the Superflexible, Hydrophobic, Silica-Based Aerogel for Thermal Insulation at Ultralow Temperature. *ACS Appl. Mater. Interfaces.* **2021**, *13* (18), 21286−21298.
(16) Viggiano, R. P.; Williams, J. C.; Schiraldi, D. A.; Meador, M. A. B. Effect of Bulky Substituents in the Polymer Backbone on the Properties of Polyimide Aerogels. *ACS Appl. Mater. Interfaces.* **2017**, *9* (9), 8287−8296.
(17) Shi, B.; Ma, B.; Wang, C.; He, H.; Qu, L.; Xu, B.; Chen, Y. Fabrication and Applications of Polyimide Nano-aerogels. *Composites Part A: Applied Science and Manufacturing.* **2021**, *143*, 106283.
(18) Deng, Y.; Pan, Y.; Zhang, Z.; Fu, Y.; Gong, L.; Liu, C.; Yang, J.; Zhang, H.; Cheng, X. Novel Thermotolerant and Flexible Polyimide Aerogel Separator Achieving Advanced Lithium-Ion Batteries. *Advanced Functional Materials.* **2022**, *32* (4), 2106176.
(19) Cheng, Y.; Zhang, X.; Qin, Y.; Dong, P.; Yao, W.; Matz, J.; Ajayan, P.; Shen, J.; Ye, M. Super-elasticity at 4 K of Covalently Crosslinked Polyimide Aerogels with Negative Poisson's ratio. *Nature communications.* **2021**, *12* (1), 4092.
(20) Meador, M. A. B.; Malow, E. J.; Silva, R.; Wright, S.; Quade, D.; Vivod, S. L.; Guo, H.; Guo, J.; Cakmak, M. Mechanically Strong, Flexible Polyimide Aerogels Cross-Linked with Aromatic Triamine. *ACS Appl. Mater. Interfaces.* **2012**, *4* (2), 536−544.
(21) Li, X.; Wang, J.; Zhao, Y.; Zhang, X. Template-Free Self-Assembly of Fluorine-Free Hydrophobic Polyimide Aerogels with Lotus or Petal Effect. *ACS Appl. Mater. Interfaces.* **2018**, *10* (19), 16901−16910.
(22) Hou, X.; Mao, Y.; Zhang, R.; Fang, D. Super-flexible Polyimide Nanofiber Cross-linked Polyimide Aerogel Membranes for High Efficient Flexible Thermal Protection. *Chem. Eng. J.*. **2021**, *417*, 129341.
(23) Yu, Z.; Dai, T.; Yuan, S.; Zou, H.; Liu, P. Electromagnetic Interference Shielding Performance of Anisotropic Polyimide/Graphene Composite Aerogels. *ACS Appl. Mater. Interfaces.* **2020**, *12* (27), 30990−31001.
(24) Ahankari, S.; Paliwal, P.; Subhedar, A.; Kargarzadeh, H. Recent Developments in Nanocellulose-Based Aerogels in Thermal Applications: A Review. *ACS Nano* **2021**, *15* (3), 3849−3874.
(25) Zhao, X.; Yi, X.; Song, J.; Yuan, X.; Yu, S.; Nie, Y.; Zhang, J.; Cao, G. Mesoporous and flexible polyimide aerogel as highly active catalytic membrane for AO7 degradation by peroxymonosulfate activation. *Chem. Eng. J.*. **2022**, *431*, 134286.
(26) Qiao, S.; Kang, S.; Zhang, H.; Yu, J.; Wang, Y.; Hu, Z. Reduced shrinkage and mechanically strong dual-network polyimide aerogel films for effective filtration of particle matter. *Separation and Purification Technology*, **2021**, *276*, 119393.
(27) Kantor, Z.; Wu, T.; Zeng, Z.; Gaan, S.; Lehner, S.; Jovic, M.; Bonnin, A.; Pan, Z.; Mazrouei-Sebdani, Z.; Opris, D.; Koebel, M.; Malfait, W.; Zhao, S. Heterogeneous silica-polyimide aerogel-in-aerogel nanocomposites. *Chem. Eng. J.*, **2022**, *443*, 136401.

https://doi.org/10.1021/acsapm.2c01180
ACS Appl. Polym. Mater. 2022, 4, 8227−8237